Response of near-inertial energy to a supercritical tropical cyclone and jet in the South China Sea: modeling study

Hiu Suet Kung, Jianping Gan*

Department of Ocean Science and Department of Mathematics, Hong Kong University of Science and Technology, Hong Kong

Corresponding author: magan@ust.hk

1   **ABSTRACT**

2   We used a well-validated three-dimensional ocean model to investigate the process of energetic

3   response of near-inertial oscillations (NIOs) to a tropical cyclone (TC) and strong background jet

4   in the South China Sea (SCS). We found that the NIO and near-inertial kinetic energy (KEni)

5   varied distinctly during different stages of the TC forcing, and the horizontal and vertical

6   transport of KEni was largely modulated by the velocity and vorticity of the jet. The KEni

7   reached its peak value within ~one-half the inertial period after the initial TC forcing stage in the

8   upper layer, decayed quickly by one-half in the next two days, and further decreased in a slower

9   rate during the relaxation stage of the TC forcing. Analyses of the KEni balance indicate that the

10   weakened KEni in the upper layer during the forcing stage was mainly attributed to the

11   downward KEni transport due to pressure work through the vertical displacement of isopycnal

12   surfaces, while upward KEni advection from depths also contributed to the weakening in the TC-

13   induced upwelling region. In contrast, during the relaxation stage as TC moved away, the effect

14   of vertical advection on KEni reduction was negligible and the KEni was chiefly removed by the

15   outward propagation of inertial-gravity waves, horizontal advection and viscous dissipation.

16   Both the outward wave propagation and horizontal advection by the jet provided the KEni source

17   in the far-field. During both stages, the negative geostrophic vorticity south of the jet facilitated

18   the vertical propagation of inertial-gravity waves.

19

1 Introduction

Near-inertial oscillations (NIOs), whose frequencies are close to the local inertial frequency contain around half of the observed internal wave kinetic energy in the ocean (Simmons and Alford, 2012). NIOs also greatly affect the kinetic energy budget in the deeper ocean as they propagate downward from the surface and enhance the mixing by increasing vertical shear (Gill, 1984; Gregg et al., 1986; Ferrari and Wunsch, 2009; Alford et al., 2016).

Tropical cyclones (TCs), with the rapid change of wind stress, provide an important generation mechanism for the NIOs. Observational studies related to a single storm or tropical cyclone (Price, 1981; Shay and Elsberry, 1987; D'Asaro et al., 1995) showed that the NIOs related to TCs can be a factor 2-3 larger than the background NIOs and last for more than 5 inertial periods (IPs). Using a hurricane-ocean coupled model, Liu et al. (2008) estimated that the energy input of tropical cyclones into the near-inertial currents was about 0.03 TW, about 10% of the total wind-induced near-inertial energy (Watanabe and Hibiya, 2002; Alford, 2003). The input of wind energy to the near-inertial band is also controlled by the translation speed of the TC (U_h) (Geisler, 1970; Price, 1981). In fact, the NIOs are largely variable during the forcing and relaxation stage of the TC forcing related to the intensity and translation speed of the TC. The variation is determined not only by the different magnitude of input of wind energy, but also by the different dynamic conditions that regulate the near-inertial kinetic energy (KEni) transport during these stages. The variable response of NIOs during different stage of TC forcing is critical for understanding the process and physics of NIOs.

Once generated, the characteristics of NIOs, in terms of the decay time scale, propagation direction, and propagation speed are influenced by various mechanisms. In linear wave theory, the β-effect leads to an equatorward propagation of the NIOs and reduces its decay time scale

43 because of the vertical propagation into deeper ocean (Gill, 1984; D'Asaro, 1989; Garrett, 2001).

44 Background flow fields also impose large influence on the evolution of NIOs. The influence of

45 background vorticity on NIOs has been observed by Weller (1982) and Kunze and Sanford

46 (1984), and proven analytically by Kunze (1985), Young and Ben Jelloul (1997), and Danioux et

47 al. (2015). Numerical study using a primitive equation model with a turbulent mesoscale eddy

48 field and uniform wind forcing gave a similar conclusion (Danioux et al., 2008). Non-linear

49 interactions also provide a mechanism for increasing the vertical wave number, thus for larger

50 vertical shear and the dissipation and dissipation and reduced decay time (Davies and Xing,

51 2002; Zedler, 2009). In addition to modifying the characteristics of the inertial-gravity waves,

52 nonlinear advection related to the front can transport NIOs away from the storm track and to

53 higher latitudes (Zhai et al., 2004). Recent observations and numerical studies in Gulf Stream,

54 Kuroshio, and Japan Sea revealed the role of vertical circulation on the generation and radiation

55 of near inertial energy (Whitt and Thomas, 2013; Nagai et al., 2015; Rocha et al., 2018; Thomas,

56 2019).

57 The South China Sea (SCS) is a region with frequent tropical cyclone occurrence, ~10

58 each year (Wang et al., 2007). Observations (Sun et al., 2011a, b; Xu et al., 2013) and numerical

59 studies (Chu et al., 2000) indicated that these TC events are sources for near-inertial energy

60 bursts. Additionally, the SCS circulation contains abundant energetic flow (e.g. Qu, 2000; Gan

61 et al., 2006; Gan et al., 2016a) and mesoscale features, such as a strong coastal jet off the

62 Vietnamese coast (e.g. Gan and Qu, 2008) and eddies (e.g. Chen et al., 2012). The distribution

63 and evolution of the TC-induced NIOs are susceptible to the influence of these background

64 currents. (Sun et al., 2011a; Sun et al., 2011b). However, the estimate of the total contribution of

65 a TC to the KEni in the SCS is difficult to obtain from observations or linear wave theory due to

66 sparse spatial observations and the non-homogenous nature of SCS circulation.

67   In this study, we apply a well-validated numerical model with specific China Sea

68 configurations to examine the response of KEni to a large TC and background stream jet over the

69 sloping topography in the SCS. A description of Typhoon Neoguri and the details of the

70 numerical model implementation are given in Section 2. In Section 3, the general characteristic

71 response of the near-inertial current and the energy fluxes during the TC forced stage and their

72 later relaxation stage as TC moved away from the concerned region are presented. Following

73 Section 3, the KEni equation is used to identify the dynamic processes of the vertical viscous

74 dissipation, pressure work, and nonlinearity during different phases of the NIOs.

75 2 Typhoon Neoguri (2008) and the Ocean Model

76 2.1 Typhoon Neoguri (2008)

77 Typhoon Neoguri formed east of the Philippines and entered the SCS on April 15. It first moved

78 west-northwest with an average translation speed of 5.8 m s^{-1} before it slowed down to 1.6 m s^{-1}

79 on April 16, based on the Joint Typhoon Warning Center (JTWC) best track data, (Fig. 1). On

80 April 17, Neoguri sped up to 3.8 m s^{-1}, turned more northward, and developed into a typhoon

81 with a maximum wind speed 51 m s^{-1} and a MSLP (minimum sea level pressure) at 948 hPa, at

82 1800 UTC on April 17 near the Xisha Islands. The Neoguri was a supercritical typhoon

83 travelling with a translation speed greater than the first baroclinic wave speed. After skirting

84 Hainan Island on April 18, Neoguri moved northward, weakened to a tropical storm, and further

85 dissipated as it moved farther inland. The NIO burst induced by Neoguri was shown by the

86 clockwise (A$_{cw}$) and counter-clockwise (A$_{ccw}$) rotary current amplitudes (m s^{-1}), from a current

87 meter mooring at Wenchang station, to the east off Hainan Island (Fig. 1c).

2.2 Ocean Model

We use the China Sea Multi-scale Ocean Modeling System (CMOMS) (Gan et al., 2016a; Gan et al., 2016b) in this study. CMOMS is based on the Regional Ocean Modeling System (ROMS) (Shchepetkin and McWilliams,2005), and the model domain covers the northwest Pacific Ocean (NPO) and the entire China Seas (Bohai, Yellow Sea, East China Sea, and SCS) from approximately 0.95ºN, 99ºE in the southwest corner to the northeast corner of the Sea of Japan. The horizontal size of this grid array decreased gradually from ~10 km in the southern part to~7 km in the northern part of the domain. Vertically, we adopted a 30-level stretched generalized terrain-following coordinate (s).

The model was forced with 6-hourly actual wind speeds of typhoon Neoguri obtained from the Cross-Calibrated Multi-Platform (CCMP) dataset, with a horizontal resolution of 0.25° (Atlas et al. (2011), ftp://podaac-ftp.jpl.nasa.gov/allData/ccmp/L3.0/flk). Wind stress is calculated based on the bulk formulation by Fairall et al. (2003). The daily mean air temperature, atmospheric pressure, rainfall/evaporation, radiation, and other meteorological variables from April 15 to April 18, 2008 from the NCEP/NCAR Reanalysis 1 were used to derive the atmospheric heat and fresh water fluxes. External forcing of depth-integrated velocities (U, V), depth-dependent velocities (u, v), temperature, T, and salinity, S, at the lateral boundaries were obtained from the Ocean General Circulation Model for the Earth Simulator (OFES) (Sasaki et al., 2008). Open boundary conditions from Gan and Allen (2005) were applied at the open boundaries.

The model was spun up from January 1, 2005 with winter initial fields (temperature and salinity) obtained from the last three-year mean fields of a 25-year run that is initialized with the World Ocean Atlas 2005 (WOA05, Locarnini et al., 2006, Antonov et al., 2006) data, and forced

111　by wind stress derived from climatological (averaged from 1988 to 2013) monthly Reanalysis of

112　10 m Blended Sea Winds released by the National Oceanic and Atmospheric Administration

113　(https://www.ncdc.noaa.gov/oa/rsad/air-sea/seawinds.htm). The dynamic configuration and

114　numerical implementation of the CMOMS system are described in detail in Gan et al. (2016a,

115　2016b).

116　　We have thoroughly validated the CMOMS by comparing simulated results with those

117　obtained from various measurements and findings in previous studies. In particular, we have

118　validated the extrinsic forcing of time-dependent, three-dimensional current system in the

119　tropical NPO, transports through the straits around the periphery of the SCS, and corresponding

120　intrinsic responses of circulation, hydrography and water masses in the SCS (Gan et al., 2016a).

121　We have also validated the circulation of CMOMS by providing a consistent physics between the

122　intrinsic responses of the circulation and extrinsic forcing of flow exchange with adjacent oceans

123　(Gan et al., 2016b). The model is also validated with available ARGO temperature profiles (not

124　shown), observed sea surface temperature (SST) and currents from a time-series current meter

125　mooring during Neoguri, as described below.

126　　Three-dimensional, hourly-mean dynamic, and thermodynamic variables from April 10

127　to May 10, 2008 were used to examine the near-inertial oscillations in this study. Because the

128　inertial period (IP) in the SCS is larger than 32 hours (near 22°N), the error induced by the

129　hourly model output is <3%.

130　**3 Model result**

131　**3.1 Characteristic response to the TC**

132　　The evolution of the response to the TC in the ocean with existence of a coastal jet in the

133　SCS is presented according to different stages of the TC forcing. During the pre-storm stage

134   (PS), before Neoguri entered the SCS on April 14, the wind stress was relatively weak (<0.1 Pa).

135   A prominent jet current separated from the Vietnamese coast flowing northeastward near 16°N

136   (Fig. 2a), and characterized the circulation in the western part of the SCS. The jet was resulting

137   from the (summer) monsoon-driven strong coastal current over narrow shelf topography off

138   Vietnam and it persisted as a distinct circulation feature in the SCS during summer. The

139   northward flowing coastal current separated from the coast and overshoots northeastward into

140   the SCS basin as it encountered the coastal promontory in the central Vietnam (Gan and Qu,

141   2008).

142   The jet formed negative (positive) geostrophic vorticity (ζ_g) to the south (north), with the

143   minimum (maximum) Rossby number (ζ_g/f) <-0.2 (>0.2) near 15.8°N (16.8°N). During the

144   forced stage (FS, Fig. 2b) between April 15 and April 19, the SCS was under the direct influence

145   of Neoguri, the wind forcing became significantly stronger (>0.1 Pa), the KE near the surface (10

146   m) intensified significantly (>500 J m^{-3}) to the east of the TC, and the coastal jet was suppressed

147   by southward flow. Meanwhile, a strong local divergence and upwelling formed in the surface

148   and generated a strong cooling (~1.5°C) belt along the TC path that lasted for more than a week.

149   The cooling zone radiated hundreds of kilometer away from the core of the TC. These features

150   were well captured by the TC-induced temperature difference between April 19 and 14 from

151   both simulated (Fig. 3a) and observed SST (Fig. 3b) (http://podaac.jpl.nasa.gov/dataset/JPL-

152   L4UHfnd-GLOB-MUR). After the end of the FS on April 20 (Fig. 2c), the jet returned to its pre-

153   storm intensity and shifted slightly northward (Fig. 2c) when the TC center approached the coast

154   (Fig. 1a). Afterwards, during the relaxation stage (RS) after April 20 (Fig. 2d), the wind forcing

155   from the TC decreased to <0.05 Pa.

156   Rotary spectra shows that the near-inertial response of surface currents to the TC

157   occurred near the local inertial frequency (f = 0.028 cph) at station Wenchang (112°E, 19.6°N)

158   during the model simulation period (April 10 – May 5) (Fig. 4). The clockwise rotary spectra is

159   calculated by:

160     $S_{cw} = 1/8(P_{uu} + P_{vv} - 2Q_{uv})$,   (1)

161   where P_{uu}, P_{vv} and Q_{uv} are auto- and quadrature-spectra, respectively (Gonella, 1972). This

162   simulated result is highly consistent with the observations in the lower frequency band. We

163   found that the correlation coefficients of near-inertial band-passed velocity between ADCP and

164   model simulation at Wenchang station were 0.62 and 0.57 for east-west (u) and north-south (v)

165   component, respectively, which indicated that the model captured reasonably well the NIOs

166   under the influence of the background circulation of the SCS. There existed inevitably the

167   model-observation discrepancies, such as differences of velocity magnitude (~0.06 m s^{-1}) at

168   near-inertial band and rotary spectra at the higher frequency (Fig. 4). The discrepancies could

169   have been caused by many reasons, such as the lack of mesoscale and sub-mesoscale processes

170   in the atmospheric forcing field, the linear interpolation process of the atmospheric forcing (Jing

171   et al., 2015), and not resolving the oceanic subscale processes by the current model resolution.

172   However, these discrepancies will not undermine the discussion about the process and

173   mechanism of near-inertial energy response to the TC and jet in this study.

174   **3.2. Near-inertial response in the upper ocean**

175   We adopted the complex demodulation method successfully used in previous NIO studies

176   (Gonella, 1972; Brink, 1989; Qi et al., 1995) to extract the inertial current signal. The simulated

177   horizontal currents ($\vec{u}_h$) were analyzed for inertial currents ($\vec{u}_i$). The inertial currents contain

178   clockwise (*cw*) and counter-clockwise (*ccw*) rotating components:

$$179 \qquad u_i + iv_i = A_{cw}e^{-i(\phi_{cw}+ft)} + A_{ccw}e^{i(\phi_{ccw}+ft)}, \qquad\qquad (2)$$

180 where u_i and v_i are the eastward and northward inertial currents at 10 m in the mixed layer, A and

181 ϕ are the amplitude and phase of the rotary currents, respectively. Subscripts represent the

182 clockwise (cw) and counter-clockwise (ccw) rotating direction, and f is the local Coriolis

183 coefficient. To obtain the amplitude and phase, we performed harmonic analysis daily with each

184 segment over one inertial period (IP). Then the rotary amplitude and phase were calculated

185 following previous studies (Mooers, 1973, Qi et al., 1995, Jordi and Wang, 2008).

186   The time evolution of the daily rotary currents during the FS and RS in the surface layer

187 varied spatially and was related to the intensity and translation speed of the TC. On April 15

188 during PS, Neoguri affected mainly the region south of 13°N, with a relatively fast translation

189 speed ($U_h > 3C_l$, Fig. 1b) and weaker intensity (V_{max}~35 m s^{-1}). In most areas, cw rotary currents

190 were strong (A_{cw} >0.1 m s^{-1}) yet decayed quickly after 3 days (<2 IP) (Fig. 5a), while the

191 magnitudes of ccw currents were very small (Fig. 5b). After April 18, Neoguri moved into the

192 region between 14°N and 18°N, where it intensified more than 40% but moved slower with

193 U_h~$2C_l$. Both the cw and ccw currents possessed larger intensities than in the southern region.

194 The induced cw currents displayed an obvious rightward bias, where the enhanced inertial

195 currents extended to ~350 km to the right of the track and to ~<150 km to the left of the track.

196 This extension of horizontal scale was related to the region with wind stress $|\tau|$>0.25 Pa in

197 Neoguri.

198   The maxima of the ccw component were located to the left of the TC's path where the

199 wind vector (Fig. 6) rotated in the same direction as the ocean currents presented in Fig. 5. The

200 connection between the right (left) bias of the cw (ccw) currents with the rotation direction of the

201 wind vector is in agreement with the explanation of Price (1981). 2-3 IPs (>6 days) after the

202   direct forcing, the *cw* currents remained significant (>0.2 m s^{-1}) in an area extending from 110°E

203   to 116°E. In contrast, the *ccw* components, which rotated in the direction of the Earth's rotation,

204   dissipated quickly after the wind forcing stopped within ~1 day. This short duration of the forced

205   inertial motion is in agreement with previous studies (Jordi and Wang, 2008).

206   Besides the intensity and duration, we also looked at the frequency shift ($\delta\omega=\omega$-f) and

207   the horizontal scale of the NIOs. The frequency shift from the local inertial frequency was

208   estimated from the temporal evolution of the phase of the back rotary current: $\delta\omega=-\partial\phi/\partial t$. In the

209   FS, the maximum frequency shift occurred near the jet (112°E to 115°E, 15°N to 16°N), where

210    $\delta\omega\approx0.08f$ ($\Delta\phi\approx\pi/4,\Delta t=3$ days, $f=4\times10^{-5}$ s^{-1} at 16°N). The horizontal scale was estimated from the

211   spatial variation of the rotary current by calculating the horizontal wave number in the

212   meridional direction as $k_y=\partial\phi/\partial y$. The largest wave number $k_y \approx 3.1 \times 10^{-5}$ rad m^{-1} was also

213   found near the jet.

214   **3.3 Characteristic near-inertial energy**

215   ***Response in the upper layer***

216   We focused on the area between 110-115°E and 13-19°N (box in Fig. 5a), defined as the

217   forced region, where the strongest NIO was produced during FS of Neoguri. We calculated the

218   wind-induced near-inertial energy flux (or the wind work) using $\vec{\tau}_i \cdot \vec{u}_i$, where $\vec{\tau}_i$ is the band-

219   passed near-inertial wind stress and $\vec{u}_i$ is the near-inertial current at the surface (Silverthorne and

220   Toole, 2009). A 4th order elliptic band-pass filter (Morozov and Velarde, 2008) was applied to

221   obtain near-inertial motion with a band ranging from $0.8f$ to $1.2f$, where f is the local Coriolis

222   coefficient. The time series of domain-averaged $\vec{\tau}_i \cdot \vec{u}_i$ over the forced region reveals that

223   significant energy input took place during the FS, with the peak value about 68×10^{-3} W m^{-2} on

224   April 17 (Fig. 7). Under this large wind energy input, the area-averaged depth-integrated KEni

225   (or *AKEni* hereafter) in the upper layer (0-30 m) increased significantly from its pre-storm value

226   to a maximum ~1500 J m^{-2} during the FS, with an increase rate of about 16×10^{-3} W m^{-2} (Fig. 7a).

227   We set 0-30 m as upper layer based on domain mean stratification and current (vorticity) vertical

228   structure. Despite the continuous positive wind energy flux, the *AKEni* in the upper layer

229   plateaued, indicating that a large amount of the wind energy was either propagating out the

230   forced region or was lost to the lower layers due to entrainment. The detailed mechanisms are

231   discussed in the following sections. After the peak of FS, the wind work decreased significantly

232   with small negative value around the end of the FS. The *AKEni* decreased to one half of its peak

233   value within 2 days (decrease rate was about 7×10^{-3} W m^{-2}). After that, the wind work was

234   almost negligible, and the decrease rate of *AKEni* became smaller (~0.8×10^{-3} W m^{-2}).

235   ***Response at depths***

236   During the FS, the *AKEni* in the upper 200 m constituted ~90% of the total *AKEni* in the

237   whole water column, while the *AKEni* between 30-200 m alone accounted for ~30-50% (Fig.

238   7b). The KENI in this mid-layer had a temporal evolution different from that in the near surface

239   layer. It reached its maximum on April 20, around one and a half days later, and was more than

240   70% of the peak value of the *AKEni* in the upper layer (~1700 J m^{-2}). Compared to the upper

241   layer *AKEni*, the the mid-layer *AKEni* during FS increased slightly more slowly (~ 4×10^{-3} W m^{-2})

242   while from April 20 to May 5 during RS it decreased much more slowly (~0.61×10^{-3} W m^{-2}),

243   and the *AKEni* became greater than that in the upper layer at the end of FS. The *AKEni* below

244   200 m was much smaller, but increased continuously from April 17 to 29, with a rate of about

245   0.62×10^{-3} W m^{-2}, which was comparable to the *AKEni* rate of decrease in the 30-200 m layer.

246   The *AKEni* in this deep layer became greater than that in the upper layer after April 25 and that

12

247   in the layer 30-200 m after April 29; the deep layer reached its maximum value ~10 days after

248   the ending of the FS.

249   Spatially, two relatively large KEni patches below upper layer were located to north and

250   south of ~16°N (Fig. 8a). Their horizontal scales, influenced by near-inertial waves, were much

251   smaller compared with those in the upper layer. The region with relatively large KEni in the

252   layer between 30-200 m located near the jet currents, with stronger value during FS than during

253   RS (Fig. 8 a,b). These results suggest that the KEni in this layer might have been determined by

254   both vertical propagation of the near-inertial gravity wave and horizontal advection of KEni of

255   the background current. Similar horizontal distribution also occurred below 200 m (Fig. 8 c,d). In

256   contrast to the layer above, the relatively large value during RS on April 30 indicated a

257   downward propagation of KEni into the deeper layer. Around the saddle zone west of the Xisha

258   Islands, a relatively large KEni below 200 m aligned with the 1000 m isobath, and might reflect

259   a topographic effect on the near-inertial wave.

260   **3.4 Vertical propagation of near-inertial energy**

261   It is clear that the distribution of the KEni was mainly controlled by the propagation of

262   near-inertial wave energy both horizontally and vertically as well as by the background jet. In

263   order to understand the KEni distribution in the deeper water inside the forced region and in the

264   far field, we selected four different locations, marked as A1, A2, C1, and C2 in Fig. 8 (a-d), for

265   the analysis of the KEni evolution during the FS and RS. Among them, A1 (113°E, 15.7°N) and

266   A2 (112.5°E, 16.9°N) are on the right side of the TC track, inside the forced region, and situated

267   about 200 km apart from each other at the northern (A2) and southern (A1) sides of the jet,

268   respectively. C1 (114.9°E, 16.9°N) and C2 (114.9°E, 18°N) are the corresponding stations in the

269   far field where relatively strong KEni intensification occurred.

270   ***Forced region (stations A1 and A2)***

271   *South of the jet at station A1*

272   The time series of the band-passed inertial velocity u_i as a function of depth shows that there was

273   an upward phase propagation, in which u_i, in the layers below 100 m was leading the upper 50 m

274   (Fig. 9a). Accompanying this phase propagation was a downward propagation of surface KEni,

275   which was represented by the lowering of the u_i maxima as a typical Poincaré wave (Kundu and

276   Cohen, 2008). There were two phases of vertical energy propagation: 1) during FS, there was a

277   rapid extension of the large u_i maxima to below 100 m from April 17 to 20, and 2) during RS,

278   the center of the large u_i value descended from ~100 m to 280 m from April 25 to May 5. The

279   vertical propagation velocity, C_{gz}, estimated from this downward transport, was ~17 m day^{-1}.

280   During the first phase, the KEni in the top 30 m and in the 30-200 m layer shared a

281   similar rate of increase on April 17, indicating that the enhancement of KEni at 30-200 m was

282   related to the entrainment between the upper and deep layer (Fig. 9c). While the KEni in the

283   upper 30 m decreased quickly from April 18, it kept increasing at depths from 30-200 m,

284   suggesting that other contributing mechanisms existed besides the entrainment. The KEni below

285   200 m also experienced notable intensification, with a smaller increasing rate than that found in

286   the 30-200 m layer (Fig. 9c). Because the viscous effect is small in the deeper water, this

287   enhancement of the KEni was most likely associated with the propagation of an inertial-gravity

288   wave.

289   During the second phase, the KEni in the 30-200 m layer decreased significantly at

290   station A1, indicating the existence of either downward or horizontal energy transport. From the

291   linearized inertial-gravity wave equation under the influence of background vorticity, C_{gz} can be

292   obtained by (Morozov and Velarde, 2008),

293 $$C_{gz} = \frac{\omega^2 - f_{eff}^2}{\omega m},\qquad(3)$$

294 where $\omega \approx 1.08f$ is the frequency with maximum S_{cw} at 200 m (Fig. 9e); $f_{eff}=f+\zeta_g/2$ is the effective

295 Coriolis coefficient; and $\zeta_g/f=-0.1$ at A1. m is the vertical wave number that we chose to be the

296 first baroclinic mode under a two-layer approximation based on the stratification (blue line in

297 Fig. 10a). From Eq. (3), C_{gz} was about 19.1 m day^{-1}, which was in the same range as the modeled

298 C_{gz}. Consistent with the case of $(\omega_0-f_{eff})/f_{eff}<0.1$ in Kunze (1985), the background vorticity in our

299 case accounted for more than 90% of the modification of the magnitude of the wave dispersion

300 property. Meanwhile, the KEni in the layer below 200 m did not increase notably, suggesting

301 that other mechanisms besides vertical propagation of the near-inertial gravity wave might have

302 been important in the evolution of KEni in water deeper than 200 m.

303 *North of the jet at station A2*

304   At location A2, strong u_i was mainly trapped in the water above 100 m, and below 100 m

305 $u_i <10$ cm s^{-1}. It returned to its pre-storm magnitude after 5 IPs (Fig. 9b). This constrain of

306 vertical propagation is likely associated with the vertical scale of the strong positive background

307 vorticity (Fig. 10b). The KEni was generally smaller than that at A1, and relatively large energy

308 was found only in the ML (Fig. 9d). C_{gz} at A2, estimated from Eq. (3), was 2.1 m day^{-1} (f_{eff}

309 $=1.08f$, $\omega \approx 1.1f$, $f=4.2\times10^{-5}$s^{-1}, and $m=2\pi/30$ m), which was about one tenth of that at A1. This is

310 consistent with the lack of a distinct pattern of vertical propagation of NIOs at this station, as

311 shown in the band-passed u_i (Fig. 9b), and the presence (absence) of a near-inertial peak of S_{cw} at

312 10 m (200 m) (Fig. 9f).

313 **Far field region (stations C1 and C2)**

314 C1 and C2 are located ~400 km to the right of the forced region. During the FS, u_i (Fig. 11a,b)

315 and KEni (Fig. 11c,d) in the upper layer were smaller than those at those stations in the forced

15

316　region due to the weaker TC influence. Only a small downward propagation was discerned

317　during the FS (Fig. 11a,b). However, notable intensification of the KEni occurred in the layers

318　below the upper layer after April 23. At C1, the S_{cw} at 10 m had a small red shift, while the S_{cw} at

319　200 and 500 m displayed blue shifts with peaks near $1.07f$ (Fig. 11e). The difference between S_{cw}

320　in the upper layer and in the layers below implies another source of KEni other than local

321　inertial-gravity wave vertical propagation.

322　　　At C2, downward energy propagation appeared after April 23, reaching 100 m from the

323　surface within 7 days, giving C_{gz} =14.3 m day^{-1} (Fig. 11b). Unlike C1, the intensification was

324　mainly in the 30-200 m layer. The S_{cw} at both 10 m and 200 m had a broad energy band near the

325　local f (Fig. 11f). Because ζ_g/f = -0.11 and f_{eff} = $1.06f$, C_{gz} estimated from Eq. (3) had an upward

326　propagation (C_{gz} =-5.4 m day^{-1}), which cannot explain the downward propagation here. The

327　linearized wave theory, with the consideration of Doppler drift due to background currents, does

328　not seem to be valid in this location. We will discuss this issue in the next section.

329　4 KEni Budget

330　We utilized the KEni equation to provide a further analysis of the source of KEni in the water

331　column. Because the horizontal component of near-inertial kinetic energy is significantly larger

332　than the vertical component (Hebert and Moum, 1994), we used the horizontal component to

333　represent the KEni. The KEni budget can be obtained from the horizontal momentum equation:

334　$$\underbrace{\frac{\partial KEni}{\partial t}}_{RATE} = \underbrace{-\vec{u}_i \cdot \langle \nabla_h p \rangle}_{PRES} \underbrace{-\rho_0 \vec{u}_i \cdot \langle \vec{u}_h \cdot \nabla_h \vec{u}_h \rangle}_{NLh} \underbrace{-\rho_0 \vec{u}_i \cdot \left\langle w \frac{\partial \vec{u}_h}{\partial z} \right\rangle}_{NLv} \underbrace{-\rho_0 \vec{u}_i \cdot \left\langle \frac{\partial}{\partial z}\left(\upsilon \frac{\partial \vec{u}_h}{\partial z} \right) \right\rangle}_{VVISC} \qquad (4)$$

335　where $KEni$ is the near-inertial energy; $\vec{u}_i$ and $\vec{u}_h$ are the near inertial velocity vector and

336　horizontal velocity, respectively; p is pressure; ρ_0 is the reference density; ∇_h is the horizontal

337　gradient operator; w is the vertical velocity; υ is the viscosity coefficient; and the angle bracket

338   represents band-passed filtering on the near-inertial band. The *PRES* term on the right side of

339   equation represents the pressure work on the *KEni*, which is associated with the inertial-gravity

340   wave propagation. NL_h and NL_v represent the horizontal and vertical divergence of energy flux

341   that include the effects of 1) the advection of *KEni* due to background currents and 2) the

342   straining of the wave field due to the background shear currents. Zhai et al. (2004) found that the

343   geostrophic advection of *KEni* contributed most of the NL_h and was the main mechanism for

344   transporting the NIOs in the absence of baroclinic dispersion of inertial-gravity waves. It was

345   also found to be more important than the dispersive processes along the Gulf Stream or shelf-

346   break jet. *VVISC* is the vertical viscous effect. As before, we integrate this equation vertically in

347   three layers: the upper layer (0-30 m), the subsurface layer (30-200 m), and the deep layer (>200

348   m). In the following sections, the *AKEni* budget is considered in entire forced region (Fig. 5) as

349   well as at the specific stations along the jet.

350   **4.1. Mean balance**

351   Figure 12 shows the time series of the *AKEni* budget over the entire forced region defined in Fig.

352   5. The time-averaged horizontal distributions of each term are presented in Fig. 13. During the

353   FS, the increase of *AKEni* in the upper layer was mainly attributed to the wind energy input

354   because the *VVISC* term was one order larger than the other terms, with a maximum of 30×10^{-3}

355   W m^{-2} on April 17 (Fig. 12a). The time-integrated *VVISC* during the FS was 2.15×10^3 J m^{-2}

356   (Table 1). Stronger *VVISC* in the upper 30 m occurred in the region between 14°N and18°N (Fig.

357   13a) along the TC track with a rightward bias, similar to the distribution of current intensity (Fig.

358   5c). Like the wind work during the FS (Fig. 7a), *VVISC* became negative after April 19,

359   indicating the *AKEni* removal by negative wind work. The influence of *VVISC* extended to the

360   30-200 m layer, and provided a positive energy flux ($\sim 1 \times 10^3$ J m^{-2}) in this layer (Figs. 12b, 13b).

361   The effect of *VVISC* in the deep layer was negligible (Fig. 12c).

362   Shortly (~1 day) after the large injection of KEni into the upper layer during the FS, the

363   *PRES* became significant (Fig. 12a, Table 1) and its horizontal distribution resembled that of

364   *VVISC* (Fig. 13a, d), suggesting that *PRES* radiated the KEni out of the forced region. It provided

365   a negative KEni flux in the upper layer (-0.65$\times 10^3$ J m^{-2}), which was largely compensated by the

366   positive flux in deeper layers (Table 1). This suggests that, during the FS, the main role of the

367   pressure work was to transport the KEni from the upper layer to the deep layers, and <15% of the

368   KEni was horizontally propagated outside the forced region.

369   During the RS, the *VVISC* was relatively small in the upper layer and it accounted for one

370   third of the *AKEni* removal in the layers below (Table 1). The *PRES* became a major sink for

371   *AKEni* in the ML (-0.85$\times 10^3$ J m^{-2}) and subsurface layer (-0.16$\times 10^3$ J m^{-2}), but was the major

372   source in the water below 200 m. The *AKEni* loss due to the horizontal wave propagation outside

373   the forced region was ~-0.42$\times 10^3$ J m^{-2}, accounting for about 40% of the total loss in the whole

374   water column.

375   Nonlinear advection terms had an important influence in the top 200 m but made little

376   contribution to the *AKEni* budget in the water below 200 m (Fig. 12, Table 1). The horizontal

377   effects of NL_h and NL_v in these layers were mainly limited to a smaller region, as compared to

378   the *VVISC* and the *PRES;* and their relatively large values occurred near the slope and the jet

379   (Figs. 13).

380   In the upper layer, NL_h advected the KEni from the source region; NL_h had positive and

381   negative values on the eastern and western sides of the TC track, respectively (Fig. 13g). Similar

382   features, but with much weaker amplitude, were found in the layers below (Fig. 13h,i). During

383   the FS, in the 30-200 m layer, the domain-averaged NL_h was positive (0.21×10^3 J m^{-2}), indicating

384   a possible extraction of the KEni from background flows. NL_v was a strong energy sink in the

385   upper 200 m (~0.64×10^3 J m^{-2}). The TC wind field generated a strong surface horizontal

386   divergence and upwelling around 16-17°N (Fig. 4b). As a result, the smaller KEni in the lower

387   layer was advected to the surface east of the Xiasha Islands. This lower KEni generated a

388   negative gradient with ambient water and resulted in the strong eastwards transport of KEni in

389   the eastward jet current. As a result, a positive NL_h center located around the area with the

390   strongest negative NL_v, and a negative NL_h center lay to the west of the positive maximum of

391   NL_h. During the RS, NL_h became negative for all layers and provided ~1/3 of the total KEni loss

392   in the water column (-0.35×10^3 J m^{-2}), while NL_v over the whole water column was significantly

393   reduced.

394   **4.2 Role of the jet**

395   We further show the distinct $AKEni$ balance in the southern and northern sides of the jet. During

396   the FS, $VVISC$ at A1 on the southern side of the jet was the dominant $AKEni$ source in both the

397   upper layer and the 30-200 m layer (Fig. 14a,b), consistent with the large vertical scale on the

398   southern side of the jet due to local negative vorticity. The enhancement of near-inertial currents

399   in the upper layer and the concurrent current divergence resulted in the vertical oscillation of

400   isopycnals (pressure) below the upper layer at this station. During this pumping process, the

401    $AKEni$ in the upper layer was partly transported downward by the $PRES$ and partly by the NL_v.

402   During the RS, the $PRES$ became the main factor in the $AKEni$ budget. It changed from source to

403   sink in the 30-200 m layer, because of less downward KEni flux from the upper layer. In the

404   deeper layer, the negative $PRES$ indicated that there was a near-inertial wave propagating away

405   from this location. The positive *AKEni* flux provided by NL_h weakened the effect of the negative

406   *PRES*.

407   During the FS at A2 on the northern side of the jet, *VVISC* in the upper layer (Fig. 14d)

408   had slightly larger magnitude than that at A1. However, it greatly decreased to 3×10^{-3} W m^{-2}

409   below the ML (Fig. 14e), which suggested that the smaller vertical scale on the northern side of

410   the jet limited the deep penetration of the wind energy in this location. Compared to A1, the NL_v

411   was much stronger in the upper layer, and about one half of the lost energy was compensated for

412   by the NL_h. The *PRES* was negligible compared to that at A1 (Fig. 14d-f). During the RS, the

413   *PRES* in the ML became a notable sink after April 21 and was accompanied by a positive NL_h

414   (Fig. 14d). This suggests that the strong jet increased the *AKEni* through either advection or

415   wave propagation due to *PRES* as a result of jet-NIO interaction at this station. In the deeper

416   layer, the *PRES* provided a positive *AKEni* flux. From the spectral analysis, the wave at 500 m

417   had a large blue shift of $>0.15f$ (Fig. 9f) that cannot be explained by the background vorticity

418   alone. The wave likely originated from the northern latitude.

419   In the far field at stations C1 and C2, where there was no direct wind forcing from the

420   TC, surface forcing (*VVISC*) was relatively small during the FS (Fig. 14g,j). Therefore,

421   horizontal transport of energy is needed to sustain the KEni intensification at these two locations

422   (Fig. 11c,d). At C1, which was on the southern side of the jet (Fig. 8) and had a negative

423   background vorticity, the *PRES* was the main source of *AKEni* in both subsurface and deep

424   layers (Fig. 14h,i). The existences of the blue shift near the local inertial frequency (Fig. 11e) and

425   of the negative background vorticity suggest the presence of a southward propagating near-

426   inertial wave towards C1 from northern region. Because C2 lies near the northeastward turning

427   point of the jet (Fig. 8), the nonlinear effect became significant in the 30-200 m layer where the

428 jet was strongest (Fig. 14k). After the enhancement of *AKEni* in the subsurface layer, the *PRES*

429 further transported the KEni downwards and became the major source for the increase of *AKEni*

430 in the deep layer after April 27 (Fig. 14l). The northeast current advected the lower frequency

431 NIO from the lower latitude towards the higher latitude, C2, which explains the red shift of the

432 NIO at this location (Fig. 11f).

5 Summary

434   TCs force the ocean to form NIOs. The response of NIOs is largely associated with the

435 different forcing stages of the TCs and background flow. Due to spatiotemporally limited

436 measurements, our understanding of the process and mechanism that govern the NIO response is

437 mainly based on theories that are constrained by idealized assumptions. In this study, we utilize a

438 well-validated circulation model to investigate the characteristic response of KEni to a

439 moderately strong TC (Neoguri) with observed strong KEni and to a unique background

440 circulation.

441   The near-inertial currents in the upper layer strengthened significantly during the TC

442 forced stage and displayed a clear rightward bias due to stronger wind forcing and the resonance

443 between the wind and the near-inertial currents. The distribution of near-inertial currents and the

444 associated rotary spectra showed that the propagation patterns of NIOs varied greatly from

445 location to location and were closely linked to the influences of the background jet.

446   We calculated the KEni balance to diagnose spatiotemporally varying responses and

447 processes of the near-inertial signals in terms of different forcing stages of the TC. Results show

448 that during the forcing period, the vertical viscous term, which represents the wind work and

449 entrainment at the base of the upper layer, was the KEni source in the upper layer. Around 0.5

450 IP after the maximum TC forcing, the pressure work became the main KEni sink in the upper

451 layer, transporting KEni in the ML into the deeper layers through inertial pumping. In the mean

452 time, upwelling caused by the TC-enhanced divergence, advected smaller KEni from deeper

453 layers to weaken the KEni in the upper layer.

454 During the TC relaxation stage, the loss of KEni in the forced region of the whole water

455 column were caused by the vertical viscous term, the pressure work, and horizontal advection

456 effects (Table 1). However, these effects acted differently in different layers. The viscous effect

457 mainly occurred inside the water column, but decreased to near zero in the upper layer after the

458 direct impact of Neoguri. The pressure work mainly transported the KEni out of the forced

459 region horizontally and out of the upper layer vertically. It was strongest on the southern side of

460 the jet, where the negative background vorticity located. The horizontal nonlinear effect also

461 contributed greatly to the KEni balance near the jet region. It acted as a major sink of KEni by

462 horizontally advecting the NIO away from the forced region. For locations away from forced

463 region, both near-inertial wave propagation and horizontal advection contributed to the

464 intensification of the KEni.

465 We examined the NIOs processes and underlying dynamics in response to different stage

466 of the TC in the semi-enclosed SCS under influence of unique and strong basin-wide circulation.

467 Unlike similar study in the SCS, this study enriches our understanding of the spatiotemporal

468 variability of TC-induced NIOs and provides a useful physical guidance for future process-

469 oriented field experiment in the SCS as well as in other subtropical marginal seas that are

470 frequently affected by the TC.

471
472 **Acknowledgments.**

References

Alford, M. H., 2003: Improved global maps and 54-year history of wind-work on ocean inertial motions. Geophys. Res. Lett., 30 (8), 1424, doi:10.1029/2002GL016614.

Alford, M. H., M. F. Cronin, and J. M. Klymak, 2012: Annual cycle and depth penetration of wind-generated near-inertial internal waves at ocean station papa in the northeast pacific. J. Phys. Oceanogr., 42, 889-908.

Alford, M.H., MacKinnon, J.A., Simmons, H.L. and Nash, J.D., 2016: Near-inertial internal gravity waves in the ocean. Annu. Rev. Mar. Sci., 8(1), 95-123.

Antonov, J. I., R. A. Locarnini, T. P. Boyer, A. V. Mishonov, and H. E. Garcia, 2006. World Ocean Atlas 2005, Volume 2: Salinity. S. Levitus, Ed. NOAA Atlas NESDIS 62, U.S. Government Printing Office, Washington, D.C., 182 pp.

Atlas, R., R. N. Homan, J. Ardizzone, S. M. Leidner, J. C. Jusem, D. K. Smith, and D. Gombos, 2011: A cross-calibrated, multiplatform ocean surface wind velocity product for meteorological and oceanographic applications. Bull. Amer. Meteor. Soc., 92, 157-174, doi:10.1175/2010BAMS2946.1.

Brink, K. H., 1989: Observations of the response of thermocline currents to a hurricane. J. Phys. Oceanogr., 19, 1017-1022.

Chen, G., J. Gan, Q. Xie, X. Chu, D. Wang, and Y. Hou, 2012. Eddy heat and salt transports in the South China Sea and their seasonal modulations, J. Geophys. Res., 117, C05021, doi:10.1029/2011JC007724.

Chu, P. C., J. M. Veneziano, C. Fan, M. J. Carron, and W. T. Liu, 2000: Response of the south china sea to tropical cyclone ernie 1996. J. Geophys. Res., 105 (C6), 13 991-14 009.

502   D'Asaro, E. A., 1989: The decay of wind-forced mixed layer inertial oscillations due to the β-

503   effect. J. Geophys. Res., 94 (C2), 2045-2056.

504   D'Asaro, E. A., C. C. Eriksen, M. D. Levine, P. Niiler, C. A. Paulson, and P. V. Meurs, 1995:

505   Upper-ocean inertial currents forced by a strong storm. part I: Data and comparisons with linear

506   theory. J. Phys. Oceanogr., 25, 2909-2937.

507   Danioux, E., P. Klein, and P. Riviere, 2008: Propagation of Wind Energy into the Deep Ocean

508   through Mesoscale Eddy Field. J. Phys. Oceanogr., 38, 2224-2241.

509   Danioux, E., Vanneste, J. and Bühler, O., 2015: On the concentration of near-inertial waves in

510   anticyclones. Journal of Fluid Mechanics, 773.

511   Davies, A. M. and J. Xing, 2002: Influence of coastal fronts on near-inertial internal waves.

512   Geophys. Res. Lett., 29 (23), 2114, doi:10.1029/2002GL015904.

513   Fairall, C. W., E. F. Bradley, J. E. Hare, A. A. Grachev, and J. B. Edson, 2003: Bulk

514   parameterization of air-sea fluxes: Updates and verification for the COARE algorithm, J.

515   Clim.,16 (4), 571–591.

516   Ferrari, R., and C. Wunsch, 2009: Ocean circulation kinetic energy: Reservoirs, sources, and

517   sinks. Annual Review of Fluid Mechanics, 41, 253-282.

518   Gan J., Z. Liu and L. Liang, 2016a: Numerical modeling of intrinsically and extrinsically forced

519   seasonal circulation in the China Seas: A kinematic study, J. Geophys. Res. (Oceans), 121 (7),

520   4697-4715, doi: 10.1002/2016JC011800.

521   Gan, J., Z. Liu and C. Hui, 2016b: A three-layer alternating spinning circulation in the South

522   China Sea, J. Phys. Oceanogr. doi:10.1175/JPO-D-16-0044.

523   Gan, J. and J. S. Allen, 2005: On open boundary conditions for a limited-area coastal model off

524   Oregon. part 1: Response to idealized wind forcing. Ocean Modelling, 8, 115-133.

525 Gan, J., H. Li, E. N. Curchister, and D. B. Haidvogel, 2006: Modeling South China Sea

526 circulation: Response to seasonal forcing regimes. J. Geophys. Res., 111 (C06034),

527 doi:10.1029/2005JC003298.

528 Gan, J., and T. Qu, 2008: Coastal jet separation and associated flow variability in the southwest

529 South China Sea. Deep-Sea Res. I, doi:10.1016/j.dsr. 2007.09.008.

530 Garrett, C., 2001: What is the "near-inertial" band and why is it different from the rest of the

531 internal wave spectrum? J. Phys. Oceanogr., 31, 962-971.

532 Geisler, J.E., 1970: Linear theory of the response of a two layer ocean to a moving hurricane.

533 Geophysical and Astrophysical Fluid Dynamics, 1, 249-272.

534 Gill, A. E., 1984: On the behavior of internal waves in the wakes of storms. J. Phys. Oceanogr.,

535 14, 1129-1151.

536 Gonella, J., 1972: A rotary-component method for analysing meteorological and oceanographic

537 vector time series. Deep-Sea Research, 19, 833-846.

538 Gregg, M. C., E. A. D'Asaro, T. J. Shay, and N. Larson, 1986: Observations of persistent mixing

539 and near-inertial internal waves. J. Phys. Oceanogr., 16, 856-885, 21.

540 Hebert, D. and J. N. Moum, 1994: Decay of a near-inertial wave. J. Phys. Oceanogr., 24, 2334-

541 2351.

542 Jing, Z., Wu, L. and Ma, X. 2015: Improve the simulations of near-inertial internal waves in the

543 ocean general circulation models. J. Atmos. Ocean. Technol., 32(10), 1960-1970.

544 Jordi, A. and D.-P. Wang, 2008: Near-inertial motions in and around the Palamos submarine

545 canyon (NW Mediterranean) generated by a severe storm. Continental Shelf Research, 28, 2523-

546 2534.

547 Kundu, P. K. and I. M. Cohen, 2008: Fluid Mechanics, 872 pp. Academic, San Diego.

548   Kunze, E., 1985: Nearinertial wave propagation in geostrophic shear. J. Phys. Oceanogr., 15,

549   544-565.

550   Liu, L. L., W. Wang, and R. X. Huang, 2008: The mechanical energy input to the ocean induced

551   by tropical cyclones. J. Phys. Oceanogr., 38, 1253-1266.

552   Locarnini, R. A., A. V. Mishonov, J. I. Antonov, T. P. Boyer, and H. E. Garcia, 2006. World

553   Ocean Atlas 2005, Volume 1: Temperature. S. Levitus, Ed. NOAA Atlas NESDIS 61, U.S.

554   Government Printing Office, Washington, D.C., 182 pp.

555   Mooers, C. N. K., 1973: A technique for the cross spectrum analysis of pairs of complex- valued

556   time series, with emphasis on properties of polarized components and rotational invariants.

557   Deep-Sea Research, 20, 1129-1141.

558   Morozov, E. G. and M. G. Velarde, 2008: Inertial oscillations as deep ocean response to

559   hurricanes. Journal of Oceanography, 64(4), 495-509, doi:10.1007/s10872-008-0042-0.

560   Nagai, T., Tandon, A., Kunze, E. and Mahadevan, A., 2015: Spontaneous generation of near-

561   inertial waves by the Kuroshio Front. J. Phys. Oceanogr., 45, 2381-2406.

562   Price, J., 1981: Upper ocean response to a hurricane. J. Phys. Oceanogr., 11(2), 153-175.

563   Qi, H., R. A. de Szoeke, and C. A. Paulson, 1995: The structure of near-inertial waves during

564   ocean storms. J. Phys. Oceanogr., 25, 2853-2871. 22.

565   Rocha, C.B., Wagner, G.L. and Young, W.R., 2018: Stimulated generation: extraction of energy

566   from balanced flow by near-inertial waves. Journal of Fluid Mechanics, 847, 417-451.

567   Sasaki, H., M. Nonaka, Y. Masumoto, Y. Sasai, H. Uehara, and H. Sakuma, 2008: An eddy-

568   resolving hindcast simulation of the quasiglobal ocean from 1950 to 2003 on the Earth

569   Simulator. In High Resolution Numerical Modelling of the Atmosphere and Ocean, K. Hamilton

570   and W. Ohfuchi (eds.), chapter 10, pp. 157–185, Springer, New York.

571   Shay, L. K. and R. L. Elsberry, 1987: Near-inertial ocean current responses to hurricane

572   Frederic. J. Phys. Oceanogr., 17, 1249-1269.

573   Shchepetkin, A. F. and J. C. McWilliams, 2005: The regional ocean modeling system: A split-

574   explicit, free-surface, topography following coordinates ocean model. Ocean Modelling, 9, 347-

575   404.

576   Silverthorne, K. E. and J. M. Toole, 2009: Seasonal kinetic energy variability of near-inertial

577   motions. J. Phys. Oceanogr., 39, 1035-1049.

578   Simmons, H. L. and M. H. Alford, 2012: Simulating the long-range swell of internal waves

579   generated by ocean storms. Oceanography, 25 (2), 30-41, doi:http://dx.doi.org/10.5670/

580   oceanog.2012.39.

581   Sun, L., Q. Zheng, D. Wang, J. Hu, C.-K. Tai, and Z. Sun, 2011a: A case study of near-inertial

582   oscillation in the south china sea using mooring observations and satellite altimeter data. Journal

583   of Oceanography, 67, 677-687, doi:10.1007/s10872-011-0081-9.

584   Sun, Z., J. Hu, Q. Zheng, and C. Li, 2011b: Strong near-inertial oscillations in geostrophic shear

585   in the northern south china sea. Journal of Oceanography, 67, 377-384, doi:10.1007/ s10872-

586   011-0038-z.

587   Thomas, L. N., 2019: Enhanced radiation of near-inertial energy by frontal vertical circulations.

588   J. Phys. Oceanogr., 49, 2407-2421.

589   Wang, G., J. Su, Y. Ding, and D. Chen, 2007: Tropical cyclone genesis over the South China

590   Sea. Journal of Marine Systems, 68, 318–326.

591   Watanabe, M. and T. Hibiya, 2002: Global estimate of the wind-induced energy flux to the

592   inertial motion in the surface mixed layer. Geophys. Res. Lett., 29, 1239,

593   doi:10.1029/2001GL04422. 23.

594   Whitt, D.B. and Thomas, L.N., 2013. Near-inertial waves in strongly baroclinic currents. J. Phys.

595   Oceanogr., 43, 706-725.

596   Xu, Z., B. Yin, Y. Hou, and Y. Xu, 2013: Variability of internal tides and near-inertial waves on

597   the continental slope of the northwestern South China Sea. J. Geophys. Res., 118, 1-15,

598   doi:10.1029/2012JC008212.

599   Young, W. R. and M. B. Jelloul, 1997: Propagation of near-inertial oscillations through a

600   geostrophic flow. Journal of Marine Research, 55, 735-766.

601   Zedler, S. E., 2009: Simulations of the ocean response to a hurricane: Nonlinear processes. J.

602   Phys. Oceanogr., 39, 2618-2634.

603   Zhai, X., R. J. Greatbatch, and J. Sheng, 2004: Advective spreading of storm-induced inertial

604   oscillations in a model of the northwest Atlantic Ocean. Geophys. Res. Lett., 31 (L14315),

605   doi:10.1029/2004GL020084.

List of Table

Table 1. Time integrated KEni budget (unit: $\times 10^3$ J m^{-2}) during the FS and RS.

List of Figures

Figure 1 (a) Track of Typhoon Neoguri (2008) from JTWC; blue square represents Wenchang where there were ADCP observations; (b) translation speed (U_h, unit: m s^{-1}) and the 1st baroclinic wave speed (C_1, unit: m s^{-1}) along the TC track; (c) clockwise (A_{cw}) and counter-clockwise (A_{ccw}) rotary current amplitude (m s^{-1}) from current measurement at Wenchang. TS: tropical storm, STS: strong tropical storm.

Figure 2 Daily mean KE (J m^{-3}, color contour) and current vectors (arrows) at 10 m (a) on April 14 of the pre-storm stage (PS), (b) on April 18 during the strongest wind forcing of the forced stage (FS), (c) on April 20 after the end of the FS, and (d) on April 30 during the relaxation stage (RS). The grey contours are the 200 m, 500 m, and 1000 m isobaths. The magenta line represents TC track. Yellow triangle on April 18 represents the TC location. The TC was located beyond the plotting domain during the other three days, as shown in Figure 1a. The velocity magnitudes<0.2 ms^{-1} are not shown in the vectors.

Figure 3: ΔSST (SSTApril 19-SSTApril14) from (a) model results and (b) GHRSST JPL MUR satellite products. The pink curve refers to the trajectory of the TC Neoguri.

Figure 4 Rotary spectra of clockwise component (upper 10 m) at Wenchang (112°E, 19.6°N) from model simulations (red) and observations (blue).

Figure 5 Time series, represented by color bar, of daily (a) clockwise and (b) counter-clockwise rotary current vectors from April 14 to 30 during different stages of the TC forcing, signifying the response of the current to the local wind rotation. For the clockwise (counter-clockwise) component, only currents with magnitude larger than 0.2 (0.05) m s^{-1} are shown. The black box represents the forced region.

Figure 6 Time series of 6-hourly wind stress vectors during the forced-stage (FS) from April 15-20.

Figure 7 Time series of (a) the area-averaged wind energy flux into the near-inertial band (unit: 10^{-3} W m^{-2}) and (b) depth-integrated KEni (J m^{-2}) in the forced region for different layers.

Figure 8 Daily averaged KEni (KJ m^{-2}) of layers (a, b) 30-200 m and (c,d) below 200 m on (a, c) April 20 during FS, and (b,d) April 30 during RS. The thick red arrows show the location of the jet (Fig. 2), while the orange curve arrows indicate regions with relative vorticity $\zeta > 0$, and the blue curve arrows indicate regions with $\zeta < 0$ induced by the jet. Stations A1 and A2 are on the right side of the TC track at the northern (A2) and southern (A1) sides of the jet, respectively. Stations C1 and C2 are corresponding stations in the far field. Station B is located in the upstream of the jet.

Figure 9 Time series of (a, b) u_i (m s^{-1}), (c, d) KEni (J m^{-2}), and (e, f) rotary spectra (cw component) at locations A1 (a,c,e) and A2 (b,d,f).

Figure 10 Time-averaged (a) N^2 (s^{-2}) and (b) low-passed (3 day) vorticity from April 15 to May 5 at locations A1 (red) and A2 (blue).

Figure 11 As in Fig. 9, except for locations C1 (a, c, e) and C2 (b, d, f).

Figure 12 Time series of area-averaged, depth-integrated KEni budget for (a) 0-30 m, (b) 30-200 m, and (c) >200 m in the forced region. Terms represent (unit: $\times 10^{-3}$ W m^{-2}): (a-c) vertical viscous effect (VVISC), (d-f) divergence of energy flux (PRES), (g-i) horizontal non-linear interaction (NL$_h$), and (j-l) vertical non-linear interaction (NL$_v$). The vertical lines separate the pre-storm stage, FS and RS during the TC forcing.

Figure 13 Horizontal distribution of time-averaged (April 15-May 5) depth-integrated KEni budget in different layers: 0-30 m (left column), 30-200 m (middle), and >200 m (right). The

terms represented are (unit: $\times 10^{-3}$ W m^{-2}): (a-c) VVISC, (d-f) PRES, (g-i) NLh, and (j-l) NLv.

Figure 14 Time series of KEni budget at locations: A1 (a-c), A2 (d-f), C1 (g-i), and C2 (j-l) in layers: 0-30 m (left column), 30-200 m (middle column), and >200 m (right column).

presented are (unit: $\times 10^{-3}$ W m^{-2}): (a-c) VVISC, (d-f) PRES, (g-i) NL$_h$, and (j-l) NL$_v$.

TERM	RATE		VVISC		PRES		NLh		NLv	
Phase	FS	RS	FS	RS	FS	RS	FS	RS	FS	RS
0-30 m	1.15	-0.97	2.15	0.00	-0.65	-0.85	-0.05	-0.10	-0.29	-0.01
30-200m	1.11	-0.44	0.96	-0.19	0.30	-0.16	0.21	-0.18	-0.35	0.10
>200 m	0.23	0.36	-0.02	-0.09	0.26	0.59	0.00	-0.07	-0.01	-0.07
Column	2.51	-1.02	3.10	-0.27	-0.09	-0.42	0.16	-0.35	-0.66	0.02

Table 1. Time integrated KEni budget (unit: $\times 10^3$ J m^{-2}) during the FS and RS.

Figure 1 (a) Track of Typhoon Neoguri (2008) from JTWC; blue square represents Wenchang where there were ADCP observations; (b) translation speed (U_h, unit: m s^{-1}) and the 1st baroclinic wave speed (C_1, unit: m s^{-1}) along the TC track; (c) clockwise (A_{cw}) and counter-clockwise (A_{ccw}) rotary current amplitude (m s^{-1}) from current measurement at Wenchang. TS: tropical storm, STS: strong tropical storm.

Figure 2 Daily mean KE (J m⁻³, color contour) and current vectors (arrows) at 10 m (a) on April 14 of the pre-storm stage (PS), (b) on April 18 during the strongest wind forcing of the forced stage (FS), (c) on April 20 after the end of the FS, and (d) on April 30 during the relaxation stage (RS). The grey contours are the 200 m, 500 m, and 1000 m isobaths. The magenta line represents TC track. Yellow triangle on April 18 represents the TC location. The TC was located beyond the plotting domain during the other three days, as shown in Figure 1a. The velocity magnitudes<0.2 ms⁻¹ are not shown in the vectors.

Figure 3 ΔSST (SST$_{\text{April 19}}$-SST$_{\text{April14}}$) from (a) model results and (b) GHRSST JPL MUR satellite products. The pink curve refers to the trajectory of the TC Neoguri.

Figure 4 Rotary spectra of clockwise component (upper 10 m) at Wenchang (112°E, 19.6°N) from model simulations (red) and observations (blue).

Figure 5 Time series, represented by color bar, of daily (a) clockwise and (b) counter-clockwise rotary current vectors from April 14 to 30 during different stages of the TC forcing, signifying the response of the current to the local wind rotation. For the clockwise (counter-clockwise) component, only currents with magnitude larger than 0.2 (0.05) m s^{-1} are shown. The black box represents the forced region.

Figure 6 Time series of 6-hourly wind stress vectors during the forced-stage (FS) from April 15-20.

(a)

Domain-Averaged $\tau_i \cdot u_i$ ($\times 10^{-3}$ W m^{-2})

(b)

Depth-Integrate KEni (J m^{-2})

Figure 7 Time series of (a) the area-averaged wind energy flux into the near-inertial band (unit: 10^{-3} W m^{-2}) and (b) depth-integrated KEni (J m^{-2}) in the forced region for different layers.

Figure 8 Daily averaged KEni (KJ m^{-2}) of layers (a, b) 30-200 m and (c,d) <200m on (a, c) April 20 during FS, and (b,d) April 30 during RS. The thick read arrows show the location of the jet (Fig. 2), while the orange curve arrows indicate regions with relative vorticity $\zeta < 0$, and the blue curve yellows indicate regions with $\zeta > 0$. Stations A1 and A2 are on the right side of the TC track at the northern (A2) and southern (A1) sides of the jet, respectively. Stations C1 and C2 are corresponding stations in the far field. Station B is located in the upstream of the jet.

Figure 9 Time series of (a, b) u_i (m s^{-1}), (c, d) KEni (J m^{-2}), and (e, f) rotary spectra (*cw* component) at locations A1 (a,c,e) and A2 (b,d,f).

Figure 10 Time-averaged (a) N^2 (s^{-2}) and (b) low-passed (3 day) vorticity from April 15 to May 5 at locations A1 (red) and A2 (blue).
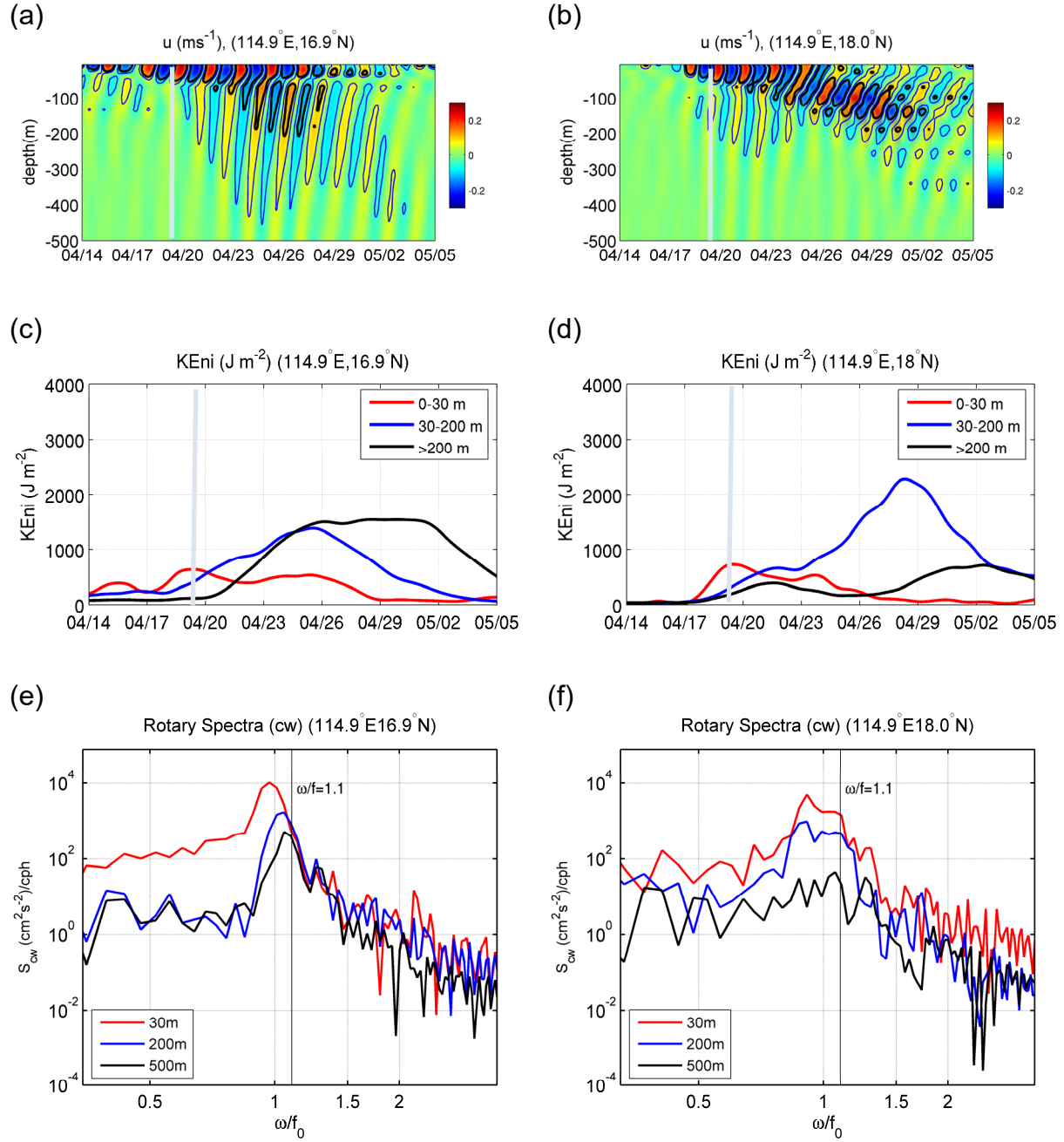
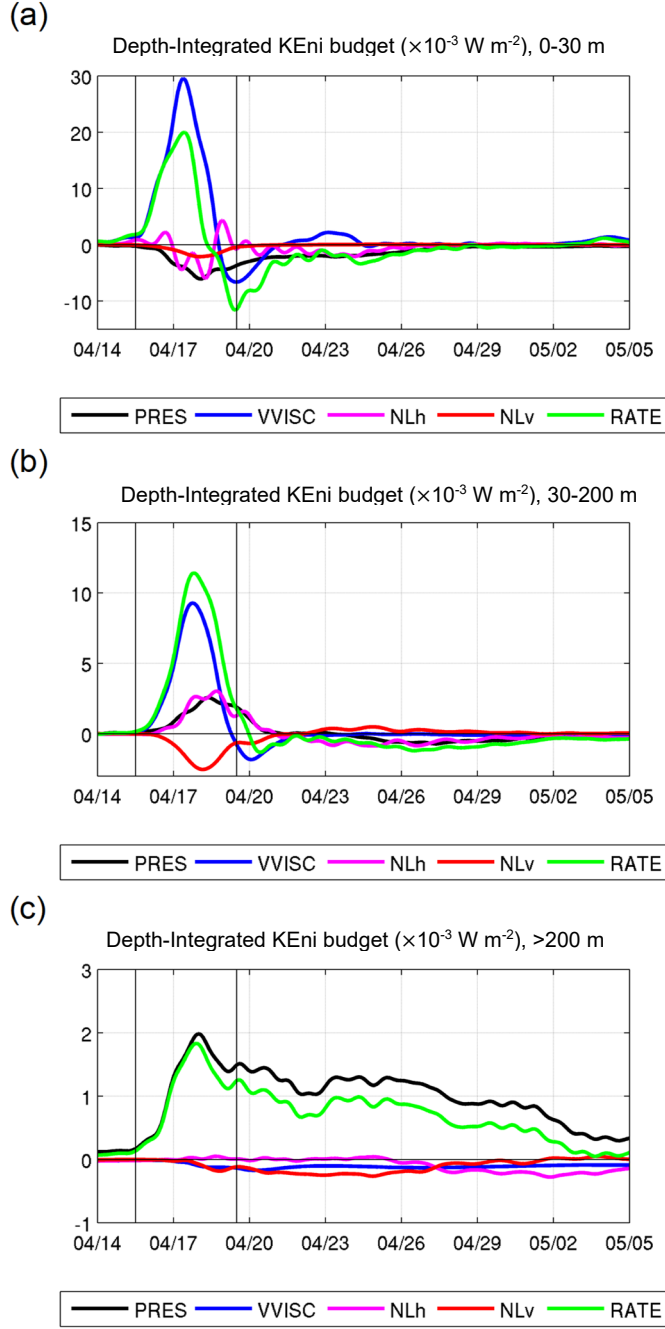Figure 11 As in Fig. 9, except for locations C1 (a, c, e) and C2 (b, d, f).

Figure 12 Time series of area-averaged, depth-integrated KEni budget for (a) 0-30 m, (b) 30-200 m, and (c) >200 m in the forced region. Terms represent (unit: $\times 10^{-3}$ W m^{-2}): (a-c) vertical viscous effect (VVISC), (d-f) divergence of energy flux (PRES), (g-i) horizontal non-linear interaction (NL$_h$), and (j-l) vertical non-linear interaction (NL$_v$). The vertical lines separate the pre-storm stage, FS and RS during the TC forcing.
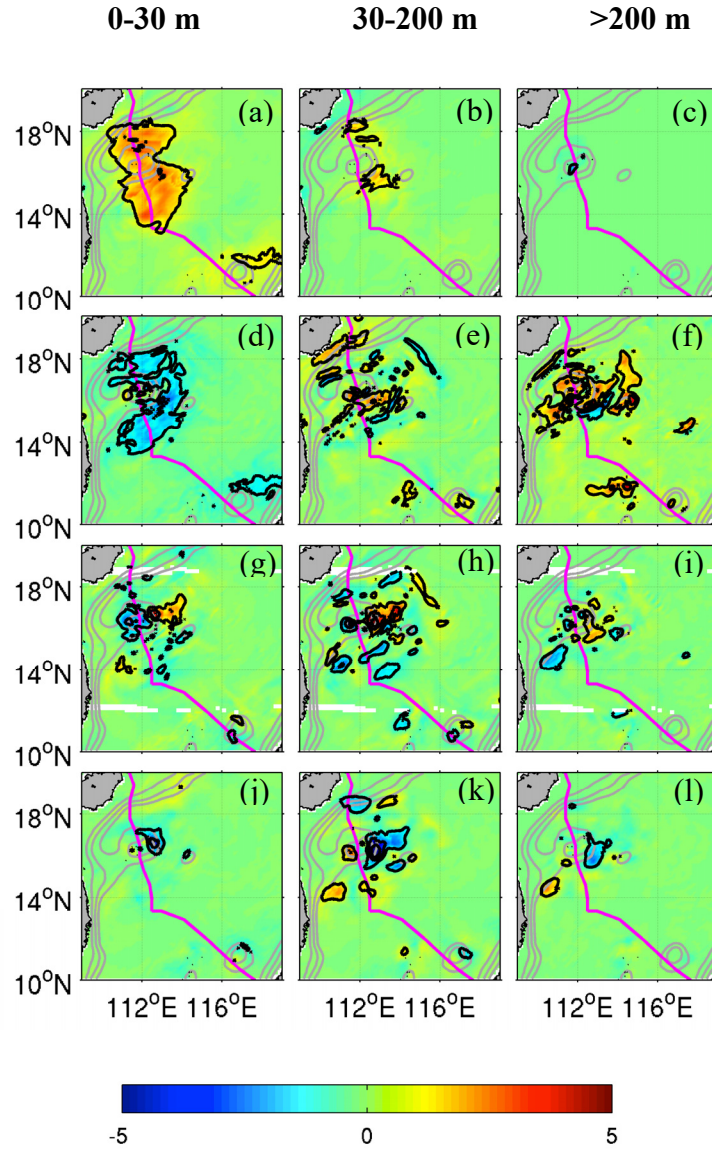
Figure 13 Horizontal distribution of time-averaged (April 15-May 5) depth-integrated KEni budget in different layers: 0-30 m (left column), 30-200 m (middle), and >200 m (right). The terms represented are (unit: $\times 10^{-3}$ W m^{-2}): (a-c) *VVISC*, (d-f) *PRES*, (g-i) *NL$_h$*, and (j-l) *NL$_v$*.
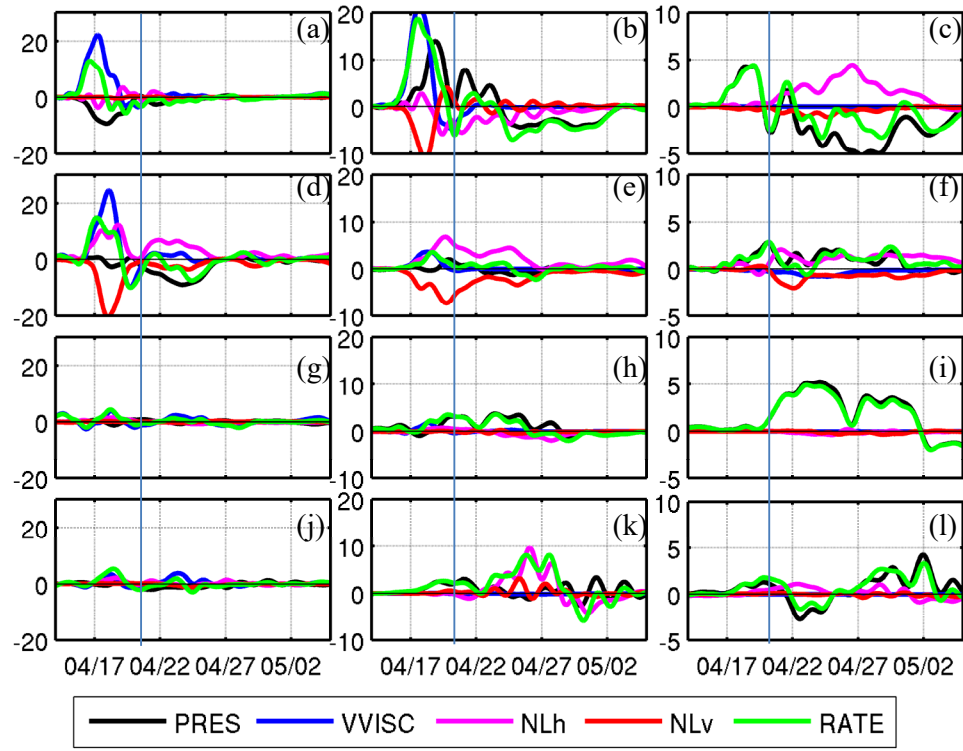
Figure 14 Time series of KEni budget at locations: A1 (a-c), A2 (d-f), C1 (g-i), and C2 (j-l) in layers: 0-30 m (left column), 30-200 m (middle column), and >200 m (right column).